metals

MDPI

Article

Tempering Behavior of a Si-Rich Low-Alloy Medium-Carbon Steel

Sergey Borisov [1,2], Yuliya Borisova [1,2], Evgeniy Tkachev [1,2], Tatiana Kniaziuk [1,3] and Rustam Kaibyshev [1,*]

[1] Laboratory of Advanced Steels for Agricultural Machinery, Russian State Agrarian University—Moscow Timiryazev Agricultural Academy, 127550 Moscow, Russia; borisov_si@bsu.edu.ru (S.B.); knyazyuk@rgau-msha.ru (T.K.)
[2] Laboratory of Mechanical Properties of Nanostructured Materials and Superalloys, Belgorod State National Research University, 308015 Belgorod, Russia
[3] National Research Center "Kurchatov Institute"—Central Research Institute of Structural Materials "Prometey", 191015 St.-Petersburg, Russia
* Correspondence: kajbyshev@rgau-msha.ru; Tel.: +7-4722-585455; Fax: +7-4722-585417

Abstract: Owing to the addition of Si, 0.33C-1.8Si-1.44Mn-0.58Cr steel exhibits a unique tempering behavior. The tempering takes place in two distinct sequential stages that are significantly different from those in steels containing 0.2–0.5 wt.% of Si. Stage I is associated with the precipitation of transition carbides in a paraequilibrium manner, can take place in temperatures ranging from ~200 to ~474 °C, and concurrently increases strength, ductility, and toughness. Stage II is associated with the decomposition of retained austenite to bainitic ferrite and transition carbides. As a result, no significant effect of overlapping of Stage I with Stage II takes place. Stage III does not occur at temperatures below ~474 °C, since the precipitation of cementite in a orthoequilibrium manner is suppressed by the addition of 1.8 wt.% of Si. It was shown that a major portion of carbon atoms redistributes to Cottrell atmospheres under quenching. During low-temperature tempering at 200–400 °C, the precipitation of transition carbides consumes a large portion of carbon atoms, thereby increasing the number of ductile fractures and improving the impact toughness without strength degradation. The formation of chains of cementite particles on boundaries takes place in Stage IV at a tempering temperature of 500 °C. This process results in the full depletion of excess carbon from a ferritic matrix that provides increased ductility and toughness but decreased strength.

Keywords: quenching and tempering; martensite; low-alloy steel; mechanical properties; microstructure; phase transformation; carbides

Citation: Borisov, S.; Borisova, Y.; Tkachev, E.; Kniaziuk, T.; Kaibyshev, R. Tempering Behavior of a Si-Rich Low-Alloy Medium-Carbon Steel. *Metals* **2023**, *13*, 1403. https://doi.org/10.3390/met13081403

Academic Editor: Frank Czerwinski

Received: 18 July 2023
Revised: 28 July 2023
Accepted: 1 August 2023
Published: 5 August 2023

1. Introduction

Low- and medium-carbon steels exhibit useful mechanical properties after quenching, followed by tempering [1,2]. Quenching produces martensite, which is highly supersaturated with carbon and other alloying elements, with a low volume fraction of retained austenite (RA) exhibiting a film-like or blocky shape [1–5]. As a result, these as-quenched steels are strong but often notably brittle [1,2,4]. Tempering leads to the decomposition of martensite and RA, thereby increasing ductility and toughness [1,2,4]. Strength typically decreases with increasing tempering temperature [1,2,4,5]. The decomposition of martensite and RA leads to the precipitation of various dispersed carbides [1–3]. Four tempering stages are usually distinguished based on isochronal tempering tests [1,2,5]. At a temperature interval of 100–250 °C, the η(Fe_2C)- or ε($Fe_{2.4}C$)-transition carbides precipitate from martensite, and this process is associated with Stage I of the tempering process. Stage II involves the decomposition of RA into ferrite and cementite precipitated on boundaries of a martensite lath structure. Stage II occurs at temperatures from 200 to 300 °C. The precipitation of lath-like cementite takes place in Stage III, which takes place at temperatures from 200 to 350 °C. The cementite particles are mainly precipitated in the martensitic matrix, but twin boundaries and boundaries of packets and prior austenite grains (PAG)

may also serve as nucleation sites for cementite [2]. These three stages overlap, and the precipitation of thermodynamically balanced cementite eventually leads to the dissolution of metastable transition carbides in accordance with the Gibbs–Thomson effect [3]. In addition, the precipitation of cementite leads to the full depletion of carbon from martensite, and a microstructure consisting of cementite and ferrite is formed [1–5]. Stage IV involves coarsening cementite at temperatures of 300–400 °C, followed by spheroidization at temperatures ranging from 400 to 600 °C [2,3]. The spheroidization of cementite is accompanied by the recovery of a martensite lath structure at T ≥ 500 °C, which leads to the formation of a tempered martensite lath structure (TMLS) [1–3]. It is worth noting that cementite particles with a nearly round shape comprise the chains along the boundaries in the TMLS.

The attractive combination of high strength, satisfactory ductility, and fracture toughness can be achieved by applying low-temperature tempering in medium-carbon, low-alloy steels [6–8]. As a modified version of AISI4340 steel (Fe–0.4C–0.7Mn–0.28Si–0.8Cr–1.8Ni–0.25Mo (wt.%)) with the addition of ~1.5 wt.% Si, 300M steel is widely used after low-temperature tempering (~305 °C) as an ultra-high-strength steel (UHSS) for critical components in the aviation industry [6–9]. Despite more than sixty years of successful commercial use, the microstructural design of this steel is poorly known [8]. It has been assumed [10] that a high Si content slows tempering, so that tempered martensite embrittlement associated with the formation of coarse cementite in the martensitic matrix is shifted to higher tempering temperatures, and the 300M steel can be tempered without embrittlement, which allows one to obtain a great yield stress (YS) in excess of 1570 MPa [1,2,8,9]. The partitioning of other substitutional elements, such as Mn and Cr, may also influence the diffusion-controlled phase transformation in Fe-C-X alloys [11].

Typical for recently developed quenching and partitioning (Q&P) steels, 300M steel exhibits a lath martensite structure with film-like RA [12,13]. The tempering behavior of 300M steel and its derivatives is a subject of discussion [6,8,9,14]. Low-temperature tempering leads to carbon partitioning from martensite to RA, which may facilitate the high strength of this steel [8,13,15]. However, interlath cementite evolves in this steel from the decomposition of the interlath RA during low-temperature tempering. The overlap between Stage I and Stage II may take place in Si-rich 300M steel in the same manner as in low-Si AISI 4340/4140 steels [5,8,15–18]. However, it is known [10,12,13,19–21] that alloying the steel with ≥1.5 wt.% Si suppresses the formation of cementite at temperatures below 400 °C. The solubility of Si in cementite is practically zero, and cementite can form if diffusion permits the redistribution of Si from cementite, followed by the depletion of Si from a 1 to 2 nm area of the ferritic matrix around the cementite, acting as a barrier for the redistribution of carbon from the diffused matrix to the growing particle [10,19–22]. The precipitation of cementite in martensite during low-temperature tempering can be suppressed by alloying with Si [1,4,19–23] or rapid tempering [16]. The suppression of Stage III prevents the formation of interlath cementite and enhances fracture toughness.

The addition of Si ≥ 1.5 wt.% to low-alloy steels shift the precipitation of cementite to temperatures ≥ 470 °C, while the diffusivity of Si is sufficient for its depletion from growing cementite particles to the ferritic matrix [19–24]. No boundary carbides precipitate in these steels up to ~450 °C; therefore, Stage I can take place up to relatively high temperatures [1–3,19,21,24]. The contents of substitutional elements in transition carbides and the martensitic matrix were nearly the same [19,24]. While the above studies highlight the effect of the addition of Si on the precipitate characteristics and mechanical properties of the steels after low-temperature tempering, the present study clarifies the concurrent processes of microstructural evolution that occur in the Si-rich steel with the increasing of the tempering temperature. Thus, the aim of the present study was to investigate the tempering behavior of UHSS steel with 1.85 wt.% Si. In this paper, specific attention will be paid to clarifying the role of Si in the overlap of the tempering stages and analysis of precipitation sequences.

2. Materials and Methods

The chemical composition of the experimental steel is listed in Table 1. The steel was produced by air induction melting followed by electro-slag remelting. Next, the steel was subjected to solution treatment at 1150 °C for 4 h, followed by forging at temperatures from 1150 to 950 °C into billets with dimensions of 60 × 150 × 450 mm^3, with subsequent air cooling. The samples with 3 mm thickness were machined from the billets and subjected to austenitization at 900 °C for 5 min, followed by hot water quenching. Isochronal tempering was carried out at 200, 280, 400, and 500 °C to reveal the microstructural changes and mechanical response in detail.

Table 1. Chemical composition of the steel in wt.%.

Fe	C	Si	Mn	Cr	N	P	S
Balance	0.33	1.85	1.44	0.58	0.0084	≤0.01	≤0.007

Hardness was measured using a Wolpert Wilson 600 MRD (Illinois ToolWorks Inc., Norwood, MA, USA) tester in accordance with ASTM E18 standard at room temperature. Ten indentations were performed on each sample to ensure the data reliability. The standard flat specimens with a gauge length of 35 mm and a cross-section of 7 × 3 mm^2 were machined by an electric discharge wire machine and then tensioned using an Instron 5882 testing machine (Illinois ToolWorks Inc., Norwood, MA, USA) at room temperature and a constant loading rate of 1 mm/min in accordance with ASTM E08M-04 standard. The elongation and reduction in cross section area of the specimens during tensile tests were measured using non-contact digital image correlation (DIC) method. Standard CVN specimens were tested at room temperature using the Instron SI-1M impact machine with a maximum energy capacity of 450 J, equipped with the Instron Dynatup Impulse data acquisition system (Instron corporation, Grove City, PA, USA) following the ASTM E-23 standard.

The structural characterization was carried out using a Quanta 600 FEG scanning electron microscope (SEM) (FEI Corporation, Hillsboro, OR, USA) equipped with an electron backscatter diffraction (EBSD) detector. The EBSD data were then analyzed using TSL–OIM software (version 6.2, TexSEM Laboratories, Draper, UT, USA). The OIM images were subjected to a clean-up procedure, setting the minimal confidence index to 0.1. The low- (LAB) and high-angle (HAB) boundaries were defined with misorientations of $2^\circ \leq \theta < 15^\circ$ and $\theta \geq 15^\circ$, respectively. The transmission electron microscopy (TEM) images were recorded with a JEOL JEM-2100 (JEOL Ltd., Tokyo, Japan) microscope equipped with an INCA energy dispersive X-ray spectrometer (EDS). The foils for TEM studies were prepared by double-jet electro-polishing technique using a solution of 10% perchloric acid in glacial acetic acid under a voltage of 21.0 V at an ambient temperature. The specimens for SEM observations were mechanically polished and then electropolished using the same electrolyte. The density of lattice dislocation, ρ_{TEM}, was estimated by counting individual dislocations in the lath interiors on TEM micrographs [19]. In addition, the densities of lattice dislocations were calculated from misorientation maps obtained by EBSD technique using Kernel misorientation. The fracture surfaces of the tension and CVN specimens were observed using the Quanta 600 FEG SEM. Other details of structural and mechanical characterization were reported in previous works [19,24–26].

The volume fraction of RA was determined by magnetic saturation measurements using a Fischer Feritscope FMP30 (Helmut Fischer Gmbh, Sindelfingen, Germany). Differential scanning calorimetry (DSC) was performed using a SDT Q600 (TA Instruments New Castle, DE, USA) calorimeter. The mass of sample was 50 mg, and a protective atmosphere of pure argon was used. The sample for DSC analysis was initially austenitized at a temperature of 900 °C and finally water-quenched. The DSC measurements were performed with a constant heating rate of 10 °C/min in the temperature range of 20–900 °C. The dilatometric curve was obtained during cooling from 900 °C to room temperature at a

cooling rate of 100 °C/s using Bahr DIL 805 dilatometer (TA Instruments New Castle, DE, USA) on cylindrical samples with a 10 mm length and a 3 mm diameter.

3. Results

3.1. DSC Analysis, Dilatometry, Magnetic Saturation Measurements

The obtained DSC curve (Figure 1a) is typical for high-Si low-alloy steels [19,24]. Weak exothermic peaks attributed to carbon clustering and precipitation of transition carbides appear at ~71 °C and ~297 °C, respectively. The onset of the last exothermic reaction takes place at ~200 °C and could also be attributed to decomposition of RA (Table 2) [19,24]. It seems that Stage I overlaps with Stage II. The distinct exothermic peak associated with the precipitation of cementite is observed at ~475 °C [19,22,24]. The data confirm that the addition of 1.85 wt.% Si shifts the onset of cementite precipitation by ΔT~200K [1–3,19,24]. The DSC data show no evidence for the precipitation of other phases at temperatures of 200–474 °C. The A_{C1} and A_{C3} temperatures [1–3] were determined from the DSC curve as 758 °C and 817 °C, respectively. Therefore, austenitizing at 900 °C provides a fully austenitic structure before quenching.

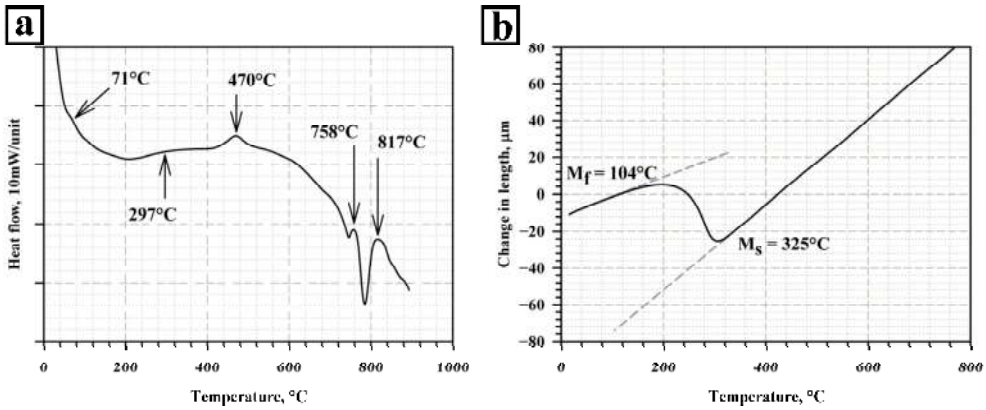

Figure 1. DSC curve (**a**) and dilatation curve (**b**).

Table 2. Microstructural parameters of the steel after quenching and tempering.

Tempering Temperature, °C/Structural Characteristics	20	200	280	400	500
PAG size, µm			26.4 ± 3.3		
Packet size, µm	2.8 ± 0.5	3.7 ± 0.6	3.1 ± 0.5	3 ± 0.5	4.2 ± 0.6
Block thickness, µm	0.6 ± 0.2	0.9 ± 0.2	0.7 ± 0.2	0.6 ± 0.2	1 ± 0.2
Mean spacing between HABs, µm	0.8 ± 1.1	1.2 ± 0.2	1.2 ± 0.2	1 ± 0.2	1.5 ± 0.2
Lath thickness, nm	175 ± 20	190 ± 15	205 ± 25	215 ± 20	230 ± 30
ρ_{TEM}, $m^{-2} \times 10^{14}$	2.7 ± 0.6	2.7 ± 0.7	2.6 ± 0.4	2.1 ± 0.5	2 ± 0.5
ρ_{KAM}, $m^{-2} \times 10^{14}$	10	7.8	8.6	7.2	7
Dimensions of carbide, nm *	-	60/7	71/13	104/13	55/29
RA fraction, %	1.6 ± 0.1	1.6 ± 0.3	0.6 ± 0.5	0	0

* Numerator and denominator are the length and thickness, respectively, of transition carbides (200–400 °C) and cementite (500 °C).

The martensite-start, M_S, and martensite-finish, M_F, temperatures were determined from the dilatation curve (Figure 1b) as 325 °C and 104 °C, respectively. Despite the water quenching producing a martensitic structure with a small fraction of RA, the dilatometric data are correlated well with the change in the volume fraction of this phase measured using the magnetic saturation method (Table 2).

3.2. Microstructure and Carbides

Typical microstructures of the steel after water quenching are presented in Figure 2 and the structural parameters are summarized in Table 2. It can be seen that the lath martensite structure exhibits a typical three-level hierarchy in its morphology, i.e., PAGs, packets, and blocks [27,28]. Film-like RA is observed at the lath and block boundaries (Figure 2d,e). PAGs and packets exhibit round and rectangular shapes, respectively (Figure 2b,c). There are two important features of the martensite lath structure. The first feature is a large fraction of HABs (Table 2). The block boundaries are mainly HABs and the average distance between these boundaries is relatively small. The distance between HABs is smaller than the packet size by a factor of ~4 and is ~30% larger than the mean block width. The nanotwins [19] are also observed within the laths in some packets. The second feature is the small lath thickness. No carbides were found in the as-quenched condition of the steel.

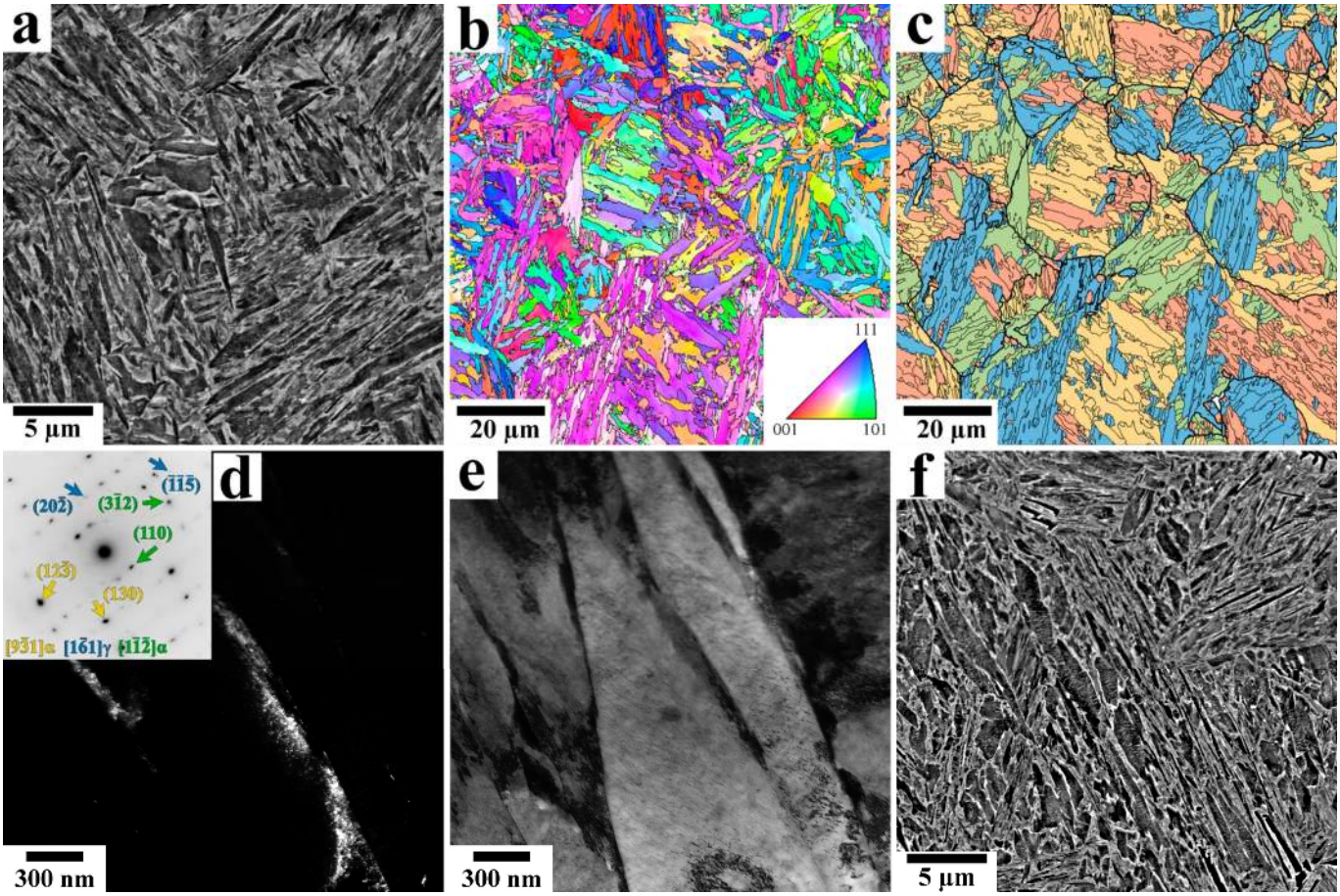

Figure 2. SEM micrograph (**a**), misorientation maps (**b**,**c**) and TEM images (**d**,**e**) of the as-quenched steel and SEM micrograph after isochronal tempering at 280 °C (**f**).

It is known [10,19,28–30] that carbon atoms tend to be trapped in Cottrell atmospheres by free lattice dislocations and interfacial dislocations composing lath boundaries. The highest fraction of carbon segregates at the lath boundaries [10,19,28–32]. The density of free dislocations, ρ_{TEM}, is presented in Table 2. The density of interfacial dislocations composing lath boundaries could be calculated using the following equation for highly elongated subgrains [33,34]:

$$\rho_{lath} = \frac{3\theta_{lath}}{b \cdot d_{lath}} \quad (1)$$

where θ_{lath} = 1.5° was taken from reference [35] as an average misorientation of lath boundaries, b = 0.258 nm is the magnitude of the Burgers vector in ferrite, and d_{lath} is the

lath thickness taken from Table 2. The ρ_{lath} value of 1.8×10^{15} m^{-2} was calculated and this value is higher than the density of free dislocations by a factor of ~7. These calculations support the simplified model suggested in reference [28] based on the presumption that almost all carbon atoms in martensite tend to segregate in the lath boundaries and the lath thickness, d_{lath}, has to ensure a complete carbon segregation in the lath boundaries to minimize the strain energy produced by the lattice distortions around the carbon atoms. The effective carbon content available for segregation in the lath boundaries could be evaluated by the following relationship, that incorporates the mean lath thickness, d_{lath} [28]:

$$l_c = \sqrt{\frac{d_{lath}}{d_{Cottrell}}}b \quad (2)$$

$$X_{LB} = \left(\frac{b}{l_c}\right)^3 \quad (3)$$

where l_C is the mean carbon spacing and $d_{Cottrell}$~7 nm is the thickness of a Cottrell atmosphere [32]. X_{LB} = 0.008, calculated from Equations (2) and (3), is the atomic fractions of carbon within the lath boundaries, and X_C = 0.0152 is the total carbon content in at.% in the steel. The portion of carbon segregated in the lath boundaries in the form of Cottrell atmospheres, V_{LB}^C, can be calculated as:

$$V_{LB}^C = \frac{X_{LB}}{X_C} \quad (4)$$

The $V_{LB}^C = 53\%$ value was obtained from Equation (4). Assuming the Cottrell atmospheres evolve on free dislocations within laths, the total portion of carbon trapped in Cottrell atmospheres will be 61% and carbon remnant is ~0.6 at.%. It is known [28,31] that the carbon content in a martensitic matrix has to be <0.22 at.% and, therefore, the density of the interfacial and free dislocations is not high enough to trap all the available carbon in the Cottrell atmospheres. Furthermore, 0.38 at.% C may be trapped as segregations in HABs and films of RA [29,36]. In general, the high density of dislocations and HABs provides a number of sites which can trap the major portion of carbon atoms. It was suggested that the carbon trapping at the defects may suppress or strongly retard the cementite formation under tempering [10].

Tempering at temperatures of 200–400 °C leads to insignificant changes in the lath thickness, the density of free dislocations, and the HAB spacing (Table 2). The precipitation and coarsening of transition η-Fe_2C carbides is observed (Figure 3a, Table 2). After tempering at 200 °C, these particles exhibit a plate-like shape with a diameter-to-thickness aspect ratio (AR) of ~9 and, therefore, diffusion-controlled lengthening can be considered as the main coarsening mechanism [3]. In the temperature interval of 200–280 °C, the thickening mechanism is operative and provides an increase in the thickness of η-Fe_2C carbide plates by a factor of ~2 and a decrease in AR to ~6 (Figure 3a,b, Table 2). The thickening of carbides correlates with the decomposition of RA, resulting in the formation of coarse plates of the η-Fe_2C particles in bainitic ferrite (Figure 3b).

In the temperature range of 280–400 °C, the lengthening of transition carbides becomes the single coarsening mechanism that leads to an increase in AR value up to ~8 (Figure 3c, Table 2). The full decomposition of RA takes place after tempering at 400 °C. The η-Fe_2C carbides are detected in the lath interiors after tempering at 200–400 °C (Figure 3a–c and Table 2). The diffraction spots represent the η-Fe_2C carbide with orthorhombic lattice characterized by lattice constants of a = 0.47 nm, b = 0.43 nm, and c = 0.28 nm [1,3,19,37–40]. The η-Fe_2C carbide exhibits an orientation relationship of $[100]_{\alpha'} \| [001]_{\eta} (010)_{\alpha'} \| (110)_{\eta}$ with a martensitic matrix [19,39,40] and a habit plane close to $\{130\}_{\alpha'}$ [19,37]. EDS analysis showed that the content of Si in η-Fe_2C particles and a martensitic matrix (Figure 3b) is nearly the same. Therefore, no diffusion partitioning of substitutional atoms between the η-Fe_2C carbide and martensitic matrix occurs during the nucleation and growth of the

η-Fe_2C. Stage I of tempering takes place at temperatures ranging from 200 to 400 °C. Stage II takes place at temperatures of 280–400 °C. The main feature of Stage II in the present steel is the suppression of cementite precipitation. No cementite was found in the as-quenched condition and after tempering at 200–400 °C. It is known that the precipitation of cementite during bainitic transformation can be suppressed by alloying the steel with ≥1.5 wt.% of Si [41].

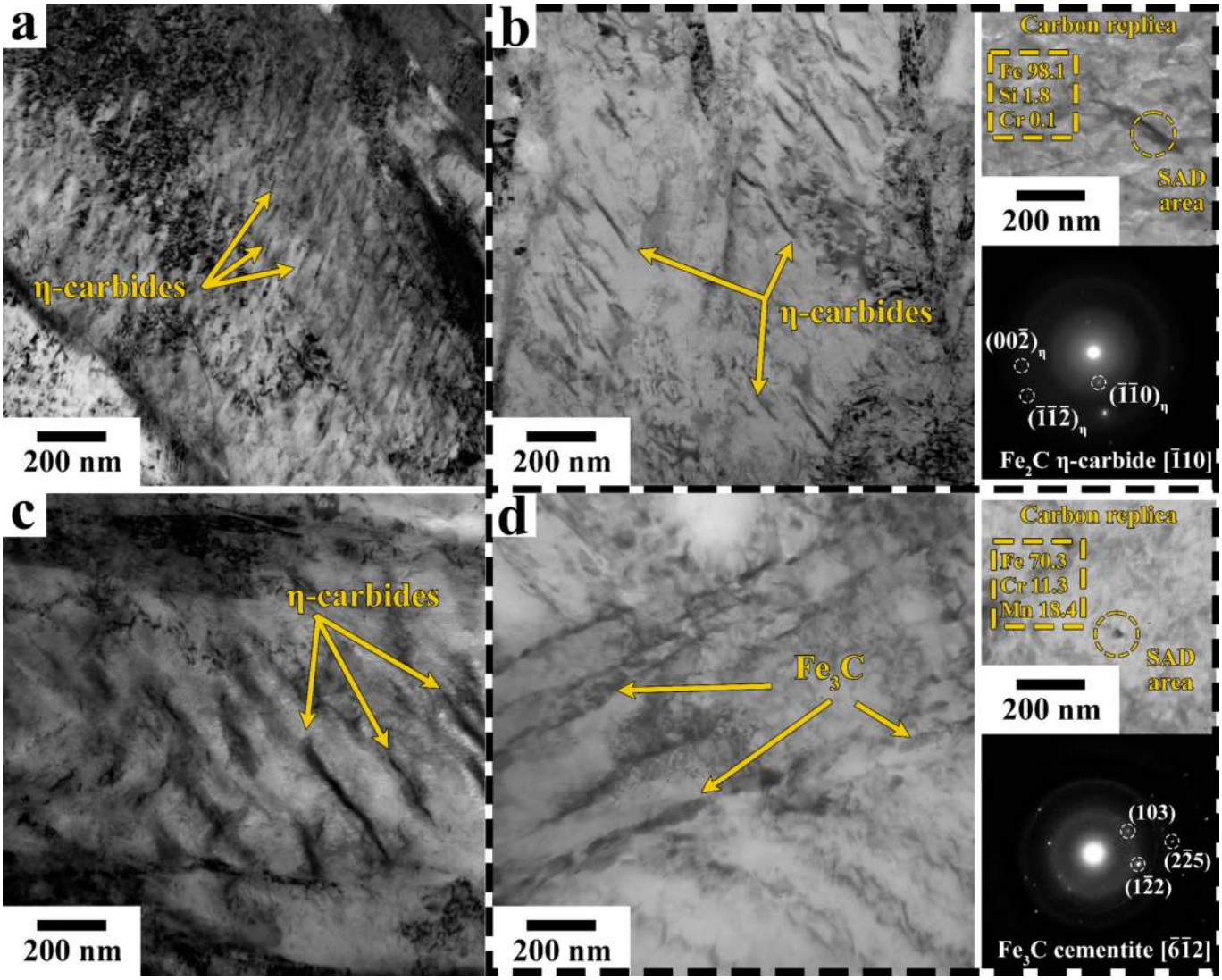

Figure 3. TEM observations after tempering at 200 °C (**a**), 280 °C (**b**), 400 °C (**c**), and 500 °C (**d**).

A further increase in tempering temperature to 500 °C leads to the precipitation of cementite particles with a round shape on the grain boundaries (Figure 3d). These carbides have nanometer dimensions (Table 2) and often locate on lath boundaries (Figure 3d). The precipitation of cementite is accompanied by the full dissolution of transition carbides (Figure 3d). It is worth noting that no cementite particles with plate-like or lath shape morphology [1–3] were found. Thus, at Stage III, the cementite can form spheroidized particles in the grain boundary regions [2]. However, these cementite particles with round shape are susceptible to Ostwald ripening [42] due to the dissolution of cementite with a plate-like shape in the matrix [2]. No matrix cementite was observed in the steel at any tempering condition and, therefore, this phase transformation could be interpreted in terms of Stage IV [1,2,4,5]. At this tempering stage, the precipitation of the cementite on the grain boundaries is followed by cementite coarsening and spheroidizing. The feature

of the present steel is the concurrent occurrence of these processes at a relatively low tempering temperature of 500 °C. As the cementite particles are mainly located at interlath and block boundaries, the coarsening and spheroidizing may be promoted by pipe and grain boundary diffusion [2,3].

Thus, the alloying of steel with 1.85 wt.% of Si expands Stage I up to T $\geq$ 400 °C, deeply changing the Stage II and suppressing the Stage III. It is obvious that the addition of 1.85 wt.% of Si leads to a two-stage precipitation sequence during tempering:

$$\text{Martensite} \rightarrow \eta\text{-}Fe_2C \rightarrow Fe_3C. \quad (5)$$

No overlap between the precipitation of the transition carbide and the cementite takes place after isochronal tempering at T $\leq$ 400 °C. The full replacement of the transition carbide particles, located in a low-carbon martensitic matrix, by boundary cementite is observed after tempering at 500 °C.

3.3. Effect of Tempering on Mechanical Properties

The engineering stress–strain curves of the steel in the as-quenched condition and after tempering are shown in Figure 4a; the hardness, yield strength (YS), ultimate tensile strength (UTS), ductility, and the product of strength and elongation (PSE) are listed in Table 3. The steel exhibits continuous yielding [1] despite the formation of Cottrell atmospheres in the as-quenched condition. The effect of tempering temperature on the strength and ductility is distinctly different in comparison with a plain carbon steel with nearly the same carbon content [2] and low-alloy steels with low Si content [1,5]. YS increases and ductility remains unchanged with increasing tempering temperature up to a tempering temperature of 280 °C, whereas no remarkable increase in YS was observed in plain carbon steel with ~0.3 wt.% C [2], and an increase in YS in AISI4340 steel was observed after tempering at 200 °C [1,5]. The peak yield strength of 1430 MPa is attained after tempering at 280 °C of the present steel, while the highest YS value of about 1240 MPa was observed in a 0.22 wt.% C steel with 0.4 wt.% Si tempered at 200 °C [43]. Therefore, alloying the steel with 1.85 wt.% Si shifts the tempering temperature corresponding to the highest YS to about 280 °C, which correlates with the formation of dense transition carbides. The strain hardening tends to decrease with increasing tempering temperature in this temperature interval and the Considère condition [3]

$$\frac{d\sigma}{d\varepsilon} = \sigma \quad (6)$$

shifts to small strains (Figure 4b). As a result, UTS tends to decrease with increasing temperature of tempering despite an increase in YS. However, an increasing tempering temperature from 200 °C to 280 °C enhances the non-uniform elongation after reaching the Considère criterion, and no effect of tempering temperature on the elongation-to-failure takes place despite a remarkable decrease in the uniform elongation (Table 3).

Table 3. Effect of tempering on mechanical properties.

Tempering Temperature, °C	YS, MPa	UTS, MPa	Elongation-to-Failure, %	PSE, GPa·%	Uniform Elongation, %	HRC
20	1230	1850	5.6	10.4	5.1	54
200	1210	1670	5.9	9.7	5.6	50
280	1430	1710	6.3	10.6	2.7	50
400	1380	1590	7.0	10.9	2.4	48
500	1130	1230	9.0	10.9	4.0	41

The ductility increases and the strength decreases gradually with an increase in tempering temperature. Similar changes in mechanical properties were observed in plain carbon and low-alloy steels with nearly the same carbon content [1,2,5]. The value of PSE

is almost independent of tempering temperature. It is worth noting that ductility tends to increase after tempering at temperatures above 280 °C and, therefore, no tempered martensite embrittlement appears.

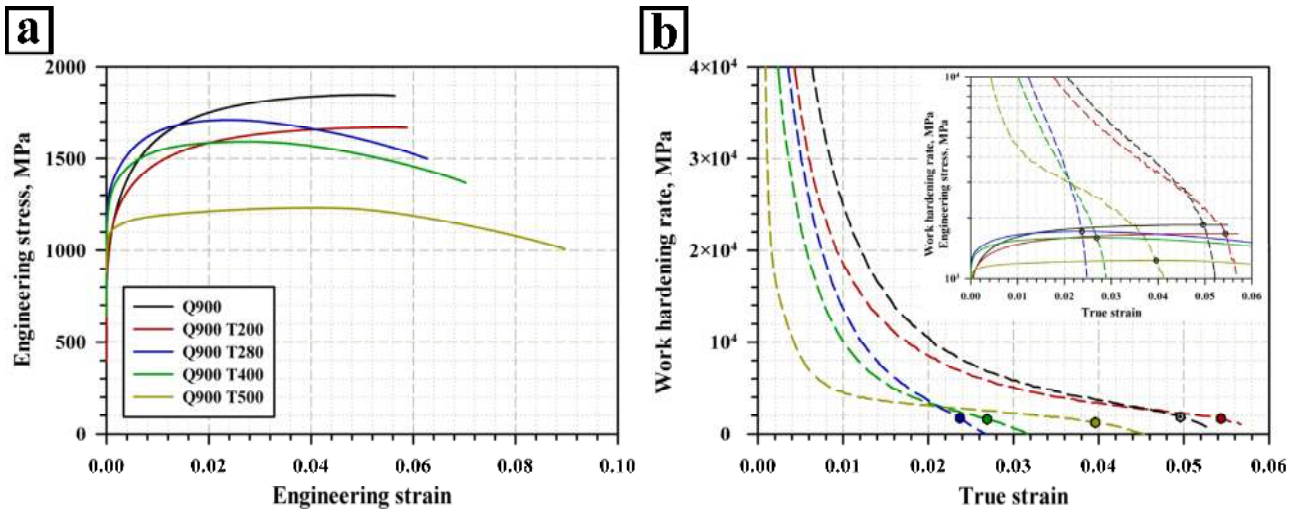

Figure 4. Engineering stress–strain curves (**a**) and strain hardening vs. strain curves (**b**).

The Charpy V-notch (CVN) impact energy generally increases with an increase in tempering temperature (Table 4). A decrease in the CVN energy at a tempering temperature of 400 °C is insignificant. Therefore, an addition of 1.85 wt.% of Si provides insignificant embrittlement of tempered martensite [9,19]. The load-deflection curves exhibit the maximum load, P_M, point, only (Figure 5a, Table 4) among the four characteristic points [19,24,44]. No evidence for the general yield load, the fast fracture load, and the fracture arrest load [19,24,44–46] could be found. In addition, no sharp decrease in the load was found during tests and, therefore, the crack propagation energy significantly contributes to the overall impact energy (Table 4).

Table 4. The CVN impact energy, the maximum load, P_M, the dynamic ultimate tensile strength, DUTS, the ductile fracture initiation energy, E_i, the fracture propagation energy, E_p, and the total fracture energy, E, calculated from CVN load–deflection curves.

Tempering Temperature, °C	*CVN*, J/cm^2	P_M, kN	DUTS, MPa	E_i, J	E_p, J	E, J
20	13	17.8	700	5.3	4.7	10
200	15	18.4	720	6.7	5.6	12.3
280	19	28.3	1120	8.8	6.6	15.4
400	17	24.7	970	7.7	5.7	13.4
500	32	31.5	1240	16.2	9.1	25

The CVN impact energy correlates with the P_M value and, therefore, tempering affects the dynamic ultimate tensile strength (DUTS), σ_{UTSd}, at which the onset of fast crack propagation takes place [19,24,44]. The DUTS values were calculated using the following relationship [19,24,44]:

$$\sigma_{UTSd} = \frac{\eta_{Pm} P_M W}{(W-a)^2 B} \quad (7)$$

where W is the specimen width (=10 mm); B is the specimen thickness (=10 mm); a is the notch depth (=2 mm); and the constraint factor at maximum force of η_{Pm} = 2.531 was taken for low alloy steels [19]. The DUTS values are presented in Table 4. It can be seen that tempering at a temperature of 280 °C provides a 60% increase in DUTS that clearly correlates with an increase in the ductile fracture initiation energy, E_i. In addition, the

increased DUTS value provides a 41% increase in the fracture propagation energy, E_p. It can be seen (Figure 5b, Tables 3 and 4) that DUTS < YS after low-temperature tempering and that the transition to brittle cleavage fracture occurs at stress smaller than YS. Therefore, low-temperature tempering increases fracture stress for brittle fracture, as expressed by the following relationship [47–49]:

$$\sigma_F = 1.41\sqrt{\frac{2E\gamma_s}{\pi(1-\upsilon^2)}}{d_{eff}}^{-1/2} \quad (8)$$

where E = 212 GPa is the Young's modulus, γ_s is the surface energy of the cleavage plane for martensitic structure, υ = 0.293 is the Poisson's ratio, and d_{eff} is the effective grain size for fracture. In general, HAB with large misorientations from $\{001\}_\alpha$ cleavage planes are effective for retarding the cleavage fracture in steels with lath martensitic structure and the distance between these boundaries could be considered as the effective grain size for fracture [47–49]. Thus, the increased fracture toughness of the low-temperature tempered steel is associated with the high brittle fracture stress.

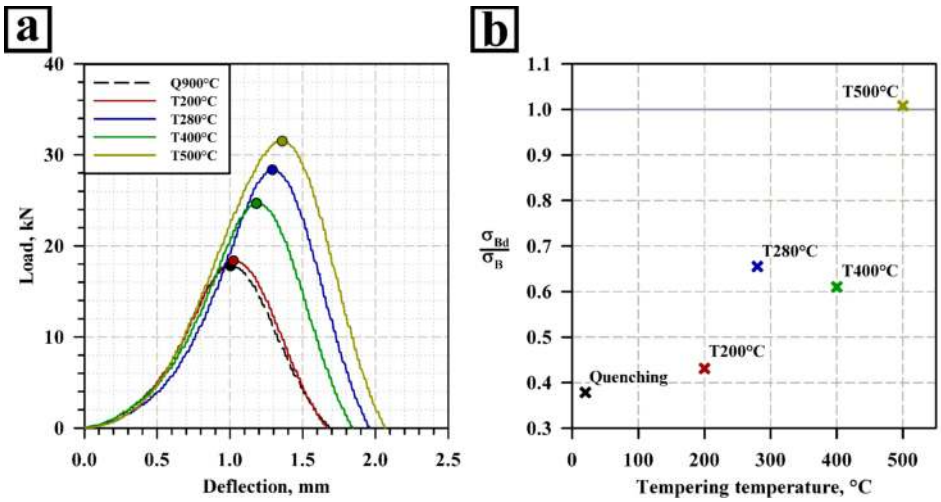

Figure 5. Load–deflection curves (**a**) and ratio of DUTS/UTS (**b**).

Tempering at 400 °C decreases DUTS insignificantly (Figure 5b, Table 4). After tempering at 500 °C, the DUTS and YS values become almost the same (Figure 5b, Tables 3 and 4). The onset of the fast crack propagation takes place at a stress sufficient for both plastic deformation in the vicinity of the crack tip and cleavage along $\{001\}_\alpha$ planes. This material condition is characterized by the highest fracture toughness associated with both increased brittle fracture stress and lowered effective YS [49].

3.4. Fractography

Three typical zones, i.e., initiation zone (IZ), fast crack propagation/fibrous zone (FCPZ), and shear-lip zone (SLZ), could be recognized on the fracture surface of CVN specimens (Figure 6c) [46,50]. The effect of tempering on the area fractions of these zones is summarized in Table 5. The fractography of the CVN specimens is presented in Figure 6. The dimple fracture is observed in IZ after quenching (Figure 6a1). Fine and shallow dimples are observed. The quasi-cleavage fracture [1,19,24,51] takes place in FCPZ (Figure 6a2). The cleavage propagates into the matrix across "weak" and "strong" boundaries. All boundaries of PAGs and major portion of packet boundaries play the role of obstacles for cleavage propagation. The cleavage penetrates a major portion of block boundaries and even some packet boundaries. The area fraction of FCPZ is the highest. The arrest of crack propagation is observed at some block boundaries. In coarse packets, the cleavage is transmitted to parallel $\{001\}_\alpha$ planes in adjacent blocks while the tear ridges are observed at some block boundaries and, therefore, the transmission of the cleavage crack to other

$\{001\}_\alpha$ cleavage planes occurs. SLZ is observed at bottom and lateral surfaces of the CVN specimens and is characterized by ductile fracture with shallow dimples (Figure 6a3). This was considered as the main feature of Si-rich low-alloy steels [19,24]. The mechanisms of dimple fracture in IZ and SLZ are essentially the same.

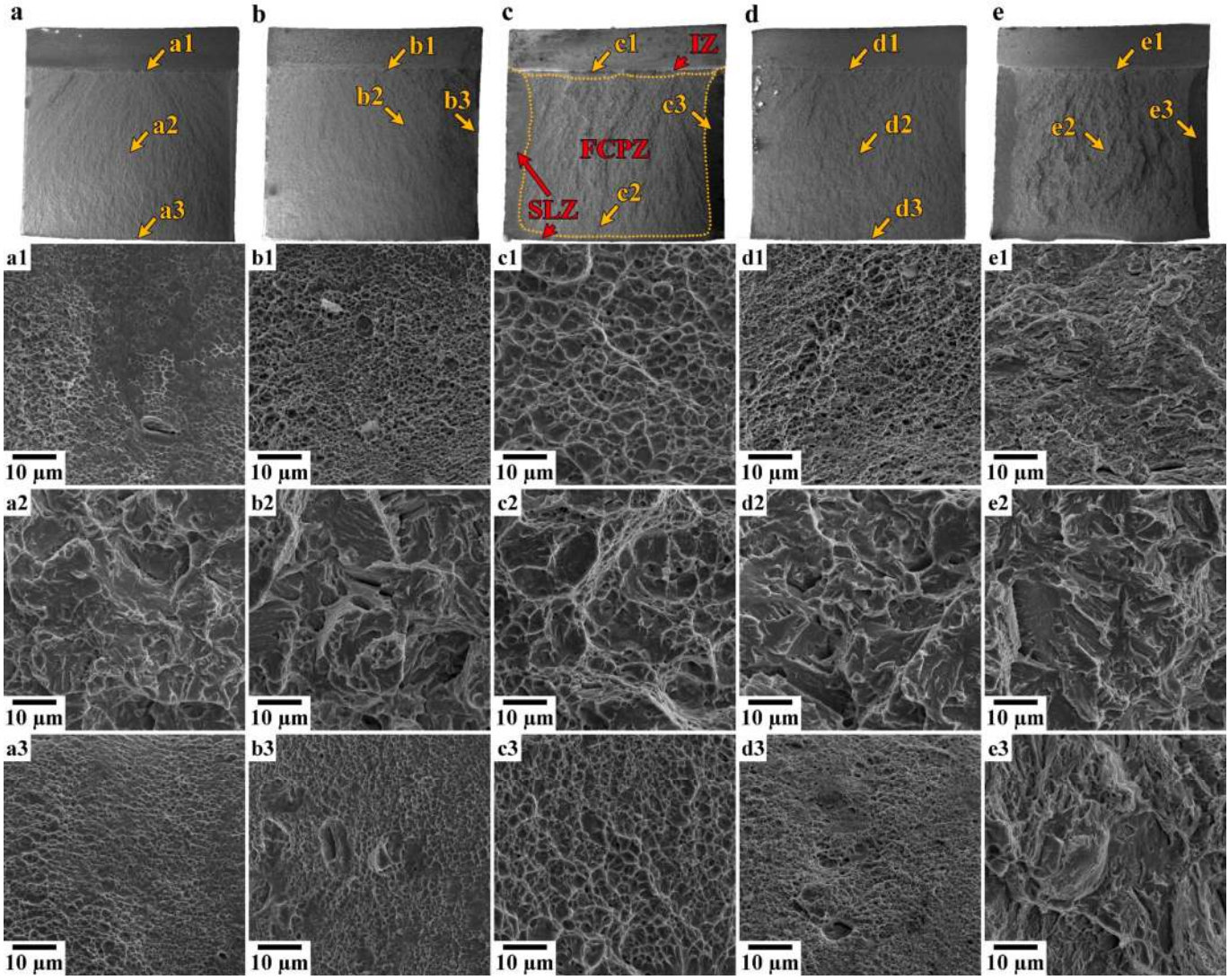

Figure 6. Low-magnification general view (**a**–**e**) and high-magnification fractographs of IZ (**a1**–**e1**), FCPZ (**a2**–**e2**), and SLZ (**a3**–**e3**) of the fracture surface in the CVN specimens in as-quenched condition (**a**–**a3**); tempering at 200 °C (**b**–**b3**); 280 °C (**c**–**c3**); 400 °C (**d**–**d3**); and 500 °C (**e**–**e3**).

Table 5. Effect of tempering on the area fractions of the initiation zone (IZ), the fast crack propagation/fibrous zone (FCPZ), and the shear-lip zone (SLZ).

Tempering Temperature, °C	IZ	FCPZ	SLZ
20	2	92	6
200	1	95	4
280	2	78	20
400	2	94	4
500	3	75	22

After tempering at 200 °C, the deep and fine dimples are observed in IZ (Figure 6b1). The major portion of block boundaries acts as obstacles for cleavage propagation in FCPZ (Figure 6b2). The refinement of effective grain size for brittle fracture takes place. The shallow and fine dimples are observed in SLZ (Figure 6b3). Tempering at 280 °C increases the depth of dimples in IZ (Figure 6c1). Very fine dimples appear at tear ridges in FCPZ (Figure 6b2). Only a minor portion of block boundaries serve as obstacles for cleavage propagation. The boundaries of PAG, packets, and some blocks play the role of obstacles for cleavage propagation in the same manner. Deep dimples appear in SLZ (Figure 6c3). The area fraction of SLZ increases. Thus, tempering at 280 °C promotes the ductile fracture and increases the brittle fracture stress, owing to the refinement of the effective grain size, d_{eff}, and increases the surface energy of cleavage plane, γ_s.

Tempering at 400 °C decreases the area fraction of IZ and SLZ (Figure 6d). The depth of dimples in IZ (Figure 6d1) is higher than that in SLZ (Figure 6d3). The number of dimples on tear ridges in FCPZ decreases (Figure 6d2). The effective grain size for brittle fracture remains almost unchanged while, in the coarse packets, the cleavage penetrates almost all block boundaries. The area fractions of the three characteristic zones after tempering at temperatures of 200 °C and 400 °C are nearly the same. After tempering at 500 °C, a decohesion along carbide/ferrite interfaces [51] is observed in IZ (Figure 6e1). Block boundaries play the role of obstacles for crack propagation in a major portion of packets in FCPZ (Figure 6e2). The area of dimples on tear ridges is small, and the portion of these areas in SLZ is large (Figure 6e3). However, the quasi-brittle fracture dominates in SLZ. The blocks play the role of effective grain size for brittle fracture in SLZ (Figure 6e3). Increasing the tempering temperature from 400 °C to 500 °C increases the fraction of SLZ by a factor of ~5. It is worth noting that the transgranular fracture is the main fracture mechanism for all steel conditions. The intergranular fracture is rarely observed after tempering at temperatures of 280–500 °C. No intergranular fracture along a structural element as a unit was found.

4. Discussion

4.1. Precipitated Carbides and Tempering Stages

It is known that the difference in diffusivity of interstitial and substitutional alloying elements in α-iron may reach ten orders of magnitude [1–3]. Two different conditions for the partitioning of these two types of elements are distinguished [2,13,23].

The first condition is termed as orthoequilibrium (OE). In this condition, the overall kinetics of precipitation and growth of carbides is governed by the slowest diffusing species, i.e., the rate of precipitation and growth of carbides is controlled by the diffusion of substitutional atoms, such as Si, Mn, and Cr in the present steel. The chemical composition of a carbide approaches the equilibrium one. The chemical compositions of martensitic/ferritic matrix and the carbides are distinctly different.

The second condition is termed as paraequilibrium (PA) [13,23]. In this condition, the overall kinetics of carbide precipitation and growth is controlled by the fastest diffusing species, such as C in the present steel. The diffusivity of carbon is high enough and this interstitial element redistributes until its content attains equilibrium in both martensite/ferrite and carbides. No partitioning of Si, Mn, and Cr between the martensite/ferrite and carbides occurs, and a growing carbide inherits the substitutional alloy contents. Thus, the contents of the substitutional elements in the martensitic/ferritic matrix and carbide are nearly the same.

The experimental data show that alloying the steel with 1.85 wt.% of Si significantly suppresses the OE precipitation and growth of cementite at tempering temperatures below 400 °C, thus modifying the tempering behavior of the steel. Increasing Si content in cementite remarkably increases the formation energy of this phase [20]. A negligible solubility of Si in cementite is associated with this fact [2,20]. It is apparent that Si $\geq$ 1.5 wt.% increases the formation energy of cementite and it becomes thermodynamically unstable [20]. The precipitation of cementite in the steels alloyed with Si $\geq$ 1.5 wt.% is only

possible in the OE condition, which shifts the precipitation of cementite to temperatures above 475 °C. OE cementite contains no Si (Figure 7a). In contrast, Cr has a strong affinity for carbon and the formation energy of cementite decreases significantly with increasing the Cr content [20], which may partially compensate for the positive effect of Si on the formation energy. The experimental observation confirms that cementite is enriched by Cr and Mn (Figures 3d and 7b), which correlates with the data reported in reference [21] and the thermodynamic calculations in Thermo-Calc with TCFE-7 steel database (Thermo-Calc software, Stockholm, Sweden), which predicts an equilibrium content of Cr and Mn equal to 10.0 at.% and 16.8 at.%, respectively. Increasing Mn content in cementite decreases its formation energy [20].

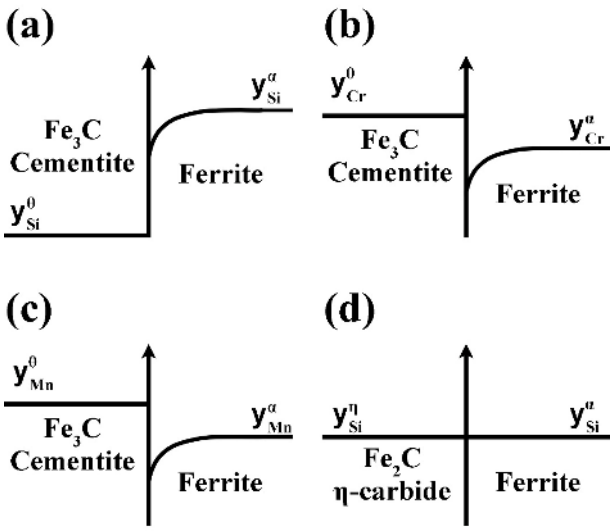

Figure 7. Schematic profiles of substitutional elements as Si (**a**,**d**), Mn (**b**), and Cr (**c**) across the transforming interface associated with (**a**–**c**) OE and (**d**) PE carbide precipitation. The *X*-axis represents distance and the *Y*-axis represents concentration. The cementite and η-Fe_2C transition carbide are the growing phases for OE and PE conditions, respectively.

In the present steel, the precipitation and growth of transition carbide occur in the PE condition (Figure 7d), which highly modifies the precipitation sequence. Table 6 gives a summary of the carbide precipitation within certain temperature ranges [19,24], and provides details of other microstructural changes in steels with Si $\geq$ 1.5 wt.% and Cr $\leq$ 0.8 wt.%. Any overlap of Stage I and Stage IV was not observed because of the aforementioned huge difference in diffusivity of the interstitial and substation elements.

In the present study, we did not obtain data on the carbon content in RA. However, it is known that the enrichment of RA by carbon takes place in 300M steel during low-temperature tempering [8,18]. Carbon partitioning between lath martensite structure and RA was found in a similar low-alloy steel with 0.53 wt.% C and 1.6 wt.% Si [52]. Tempering at temperatures of 200, 280, 400, and 500 °C provides carbon content in RA of 0.8; 1.3, 1.36, and 0.77 wt.%, respectively [52]. The volume fraction of RA in that steel in its as-quenched condition is higher by a factor of ~10 than that in the present steel. The M_S temperature attains 0 °C at a carbon enrichment of RA $\geq$ 1 wt.% and, therefore, bainitic transformation becomes a single mechanism for decomposition of RA at tempering temperatures of 280–400 °C [52]. We may anticipate the same effect of tempering temperature on the stability of RA and the mechanisms of its decomposition in the present steel (Table 6). This assumption is supported by the TEM observation of transition carbides with increased dimensions near various boundaries (Figure 3b,c).

It is known [13,53] that the carbon partitioning from a martensitic matrix to RA, in the interval of low-temperature tempering, is considered on the basis of constrained PE (CPE) condition, assuming that the carbide precipitation in martensite and the decomposition of austenite to bainite are totally suppressed. The data of the present study indicate that this

approach is oversimplified since the processes of the precipitation of transition carbides in martensite, the carbon enrichment of RA, and the decomposition of RA to bainitic ferrite and transition carbides are overlapped. The highest possible carbon enrichment of RA is governed by PE between transition carbide and austenite. The aforementioned increase in carbon content in RA, with increasing tempering temperature from 280 to 400 °C in the steel with 0.53 wt.% C, supports this assumption [52]. The precipitation of cementite is essential for carbon diffusion from RA since the equilibrium cementite solvus for austenite locates at lower carbon concentration than the metastable solvus of transition carbides [3]. Thus, the suppression of cementite precipitation is a prerequisite condition for the carbon enrichment of RA.

Table 6. Transformations occurring during tempering of lath martensite in low-alloy and medium-carbon steels with Si $\geq$ 1.5 wt.% and Cr $\leq$ 0.8 wt.%.

Tempering Temperatures, °C	Tempering Stages	Transformation	Remarks
<200	-	Carbon clustering	-
200–400	I	Precipitation of transition carbides in martensitic matrix	Transition carbides are η-Fe_2C
280–400	II	Decomposition of RA occurs through bainitic transformation and results in precipitation of transition carbides	The carbon enrichment of RA occurs. Dimensions of transition carbides precipitated during bainitic transformation of RA are higher than those precipitated from martensite
>400	IV	Precipitation, coarsening, and spheroidizing of cementite	Cementite form chains along lath, block, packet, and PAG boundaries

4.2. Mechanical Properties and Tempering Stages

Stage I of tempering provides a concurrent increase in YS and fracture toughness, while ductility remains unchanged and UTS slightly decreases. An increase in YS is attributed to the dispersion strengthening associated with the precipitation of nanosized transition carbides. An increase in the fracture toughness associated with the increased σ_F value could be attributed to two factors. The first, the γ_s value, may increase due to the depletion of carbon from a martensitic matrix, owing to the precipitation of transition carbides [47–49]. It is apparent that the depletion of carbon from Cottrell atmospheres and boundary segregations has no effect on the surface energy of $\{100\}_\alpha$ cleavage planes, and that the γ_s value is controlled by carbon content in bcc lattice [19,24,31]. The second, the effective grain size, decreases due to the transition from the Bain unit size to block size [54]. We suggest a single reason for this transition in the present steel after low-temperature tempering. It is known that film-like RA has a crack blunting effect that increases the CVN impact energy [43]. The data of the present study unambiguously establish that only film-like RA, enriched by carbon and located on block boundaries, play the role of an obstacle for crack propagation. Despite the low volume fraction of RA in the studied steel, the preferable location of thin films of this phase along the grain boundaries may impede the crack propagation effectively. The superposition of these two factors is responsible for the increased fracture toughness after Stage I.

It is worth noting that the precipitation of η-Fe_2C transition carbide facilitates crack propagation due to void formation at its interfaces [55]. However, an increase in the γ_s value and a decrease in the effective grain size compensate for this effect. An increase in the effective stress for the brittle fracture increases the contribution of ductile fracture associated with IZ, SLZ, and the energy of the crack propagation in FCPZ that enhances the fracture toughness, whereas the gradual decrease in UTS and YS, with increasing the

tempering temperature above 280 °C, is mainly associated with a progressive decrease in the dislocation strengthening.

At Stage IV, the dissolution of the matrix transition carbides decreases the contribution of dispersion strengthening, leading to a decrease in the YS and UTS values. The precipitation hardening from boundary cementite particles is significantly counteracted by a decrease in the dislocation hardening. The fracture toughness and ductility are significantly higher than those at Stage I, due to higher DUTS and increased crack initiation and crack propagation energies. However, the contribution of ductile fracture to overall fracture process is even lower than that after tempering at 280 °C, despite DUTS/UTS = 1 (Figure 5b). This fact is attributed to decohesion along the carbide/ferrite interfaces. The main reason for increased fracture toughness could be a significant increase in the γ_s value and, therefore, the effective fracture stress due to the full decomposition of martensite that increases the crack propagation energy. The boundary cementite slightly facilitates intergranular fracture, but transgranular fracture remains dominant. No embrittling agents are present in Si-rich steel with a small content of phosphorus and an average distance between HABs of ~1.5 μm. The obtained results indicate that alloying with Si is suitable for achieving good mechanical properties in low-alloyed steels subjected to low-temperature tempering that are widely used in construction, transportation, and agriculture machineries. Nevertheless, the effect of Si and C content on the stabilization of RA and the kinetics of carbide precipitation deserve further clarification to optimize the strength–toughness combination.

5. Conclusions

1. Alloying steel with ≥1.5 wt.% of Si suppresses the precipitation of paraequilibrium cementite. Only orthoequilibrium cementite may precipitate and grow in this steel, which decreases the number of tempering stages and eliminates the overlap between the precipitation of transition carbides and cementite. Stage III does not take place if cementite may precipitate due to the partitioning of substitutional atoms. Stage I, associated with the precipitation of transition carbides, expands to T ≥ 400 °C, followed by Stage IV, which is associated with the precipitation of cementite. Stage II is associated with the decomposition of retained austenite to bainitic ferrite and transition carbides. The overlap of Stages I and II has no significant effect on the dispersion of carbides.

2. The precipitation of transition carbides increases the yield stress and fracture toughness. The elongation-to-failure remains almost unchanged and ultimate tensile strength decreases at Stage I. The precipitation of cementite decreases the strength and increases the ductility and fracture toughness. The elimination of Stage III suppresses or decreases the tempered martensite embrittlement.

3. The processes of the precipitation of transition carbides and the carbon enrichment of retained austenite occur concurrently. Si addition is ineffective in the suppression of the precipitation and growth of transition carbides since these processes occur in a paraequilibrium manner. The precipitation of cementite prevents the carbon enrichment of retained austenite.

4. The block size may play a role in the effective grain size for brittle fracture if carbon-enriched film-like retained austenite is located at the block boundaries.

Author Contributions: Conceptualization, E.T. and R.K.; methodology, E.T., S.B. and Y.B.; validation, Y.B. and E.T.; formal analysis, S.B. and Y.B.; investigation, S.B., E.T., Y.B., T.K. and R.K.; resources, R.K.; data curation, E.T. and S.B.; writing—original draft preparation, E.T. and R.K.; writing—review and editing, Y.B., E.T. and S.B.; visualization, E.T.; supervision, R.K.; project administration, R.K.; funding acquisition, R.K. All authors have read and agreed to the published version of the manuscript.

Funding: This research was funded by the Ministry of Science and Higher Education of the Russian Federation, grant number 075-15-2021-572.

Institutional Review Board Statement: Not applicable.

Informed Consent Statement: Not applicable.

Data Availability Statement: Not applicable.

Acknowledgments: The studies were carried out using equipment from the Joint Scientific Center for Technologies and Materials of Belgorod State National Research University, which is supported by the Ministry of Science and Higher Education of the Russian Federation under contract No. 075-15-2021-690 (unique identifier RF—2296.61321X0030).

Conflicts of Interest: The authors declare no conflict of interest.

References

1. Krauss, G. *Steels: Processing Structure, and Performance*, 2nd ed.; ASM International: Materials Park, OH, USA, 2005. [CrossRef]
2. Bhadeshia, H.K.D.H.; Honeycombe, R. *Steels: Microstructure and Properties*, 4th ed.; Butterworth-Heinemann: Oxford, UK, 2017; ISBN 978-0-0810-0272-8.
3. Porter, D.A.; Esterling, K.E.; Sherif, M. *Phase Transformation in Metals and Alloys*, 3rd ed.; CRS Press: Boca Raton, FL, USA, 2009; ISBN 978-1-4398-8357-0.
4. Krauss, G. Tempering of lath martensite in low and medium carbon steels: Assessment and challenges. *Steel Res. Int.* **2017**, *88*, 1700038. [CrossRef]
5. Clarke, A.J.; Klemm-Toole, J.; Clarke, K.D.; Coughlin, D.R.; Pierce, D.T.; Euser, V.K.; Poplawsky, J.D.; Clausen, B.; Brown, D.; Almer, J.; et al. Perspectives on quenching and tempering 4340 steel. *Metall. Mater. Trans. A* **2020**, *51*, 4984–5005. [CrossRef]
6. Malakondaiah, G.; Srinitlas, M.; Rama Rao, P. Ultrahigh-strength low alloy steels with enhanced fracture toughness. *Prog. Mater. Sci.* **1997**, *42*, 209–242. [CrossRef]
7. Li, J.; Zhan, D.; Jiang, Z.; Zhang, H.; Yang, Y.; Zhang, Y. Progress on improving strength-toughness of ultra-high strength martensitic steels for aerospace applications: A review. *J. Mater. Res. Technol.* **2023**, *23*, 172–190. [CrossRef]
8. Euser, V.K.; Williamson, D.L.; Findley, K.O.; Clarke, A.J.; Speer, J.G. The Role of Retained Austenite in Tempered Martensite Embrittlement of 4340 and 300-M Steels Investigated through Rapid Tempering. *Metals* **2021**, *11*, 1349. [CrossRef]
9. Tomita, Y. Development of fracture toughness of ultrahigh strength, medium carbon, low alloy steels for aerospace applications. *Int. Mater. Rev.* **2000**, *45*, 27–37. [CrossRef]
10. Kozeschnik, E.; Bhadeshia, H.K.D.H. Influence of silicon on cementite precipitation in steels. *Mater. Sci. Technol.* **2008**, *24*, 343–347. [CrossRef]
11. Kuang, W.; Wang, H.; Li, X.; Zhang, J.; Zhou, Q.; Zhao, Y. Application of the thermodynamic extremal principle to diffusion-controlled phase transformations in Fe-CX alloys: Modeling and applications. *Acta Mater.* **2018**, *159*, 16–30. [CrossRef]
12. Fonstein, N. *Advanced High Strength Sheet Steels*; Springer International Publishing: New York, NY, USA, 2015. [CrossRef]
13. Speer, J.G. Phase transformations in quenched and partitioned steels in Phase Transformation in steels. In *Diffusionless Transformation, High Strength Steels, Modeling and Advanced Analytical Techniques*; Pereloma, E., Edmonds, D.V., Eds.; Woodhead Publishing Ltd.: Cambridge, UK, 2012; Volume 2, pp. 247–270.
14. Tang, Y.; Si, Y.; Yu, S.; Xu, Z.; Cao, P.; Li, S.; Zhang, L.; Li, K. Effect of Heat Treatment on Microstructure and Properties of Improved 40CrNi2Si2MoV Steel. *Steel Res. Int.* **2023**, *94*, 2200627. [CrossRef]
15. Sherman, D.H.; Cross, S.M.; Kim, S.; Grandjean, F.; Long, G.J.; Miller, M.K. Characterization of the Carbon and Retained Austenite Distributions in Martensitic Medium Carbon, High Silicon Steel. *Metall. Mater. Trans. A* **2007**, *38*, 1698–1711. [CrossRef]
16. Judge, V.K.; Speer, J.G.; Clarke, K.D.; Findley, K.O.; Clarke, A.J. Rapid Thermal Processing to Enhance Steel Toughness. *Sci. Rep.* **2018**, *8*, 445. [CrossRef] [PubMed]
17. Hunkel, M.; Dong, J.; Epp, J.; Kaiser, D.; Dietrich, S.; Schulze, V.; Rajaei, A.; Hallstedt, B.; Broeckmann, C. Comparative Study of the Tempering Behavior of Different Martensitic Steels by Means of In-Situ Diffractometry and Dilatometry. *Materials* **2020**, *13*, 5058. [CrossRef] [PubMed]
18. Euser, V.K.; Williamson, D.L.; Clarke, A.J.; Speer, J.G. Cementite Precipitation in Conventionally and Rapidly Tempered 4340 Steel. *JOM* **2022**, *74*, 2386–2394. [CrossRef]
19. Tkachev, E.; Borisov, S.; Belyakov, A.; Kniaziuk, T.; Vagina, O.; Gaidar, S.; Kaibyshev, R. Effect of Quenching and Tempering on Structure and Mechanical Properties of a Low-Alloy 0.25C Steel. *Mater. Sci. Eng. A* **2023**, *868*, 144757. [CrossRef]
20. Bhadeshia, H.K.D.H. Cementite. *Int. Mater. Rev.* **2020**, *65*, 1–27. [CrossRef]
21. Wu, Y.X.; Sun, W.W.; Gao, X.; Styles, M.J.; Arlazarov, A.; Hutchinson, C.R. The effect of alloying elements on cementite coarsening during martensite tempering. *Acta Mater.* **2020**, *183*, 418–437. [CrossRef]
22. Forsik, S.A.; Rivera-Diaz-Del-Castillo, P.E. Martensitic Steels: Epsilon Carbides in Tempered. In *Encyclopedia of Iron, Steel, and Their Alloys*; Taylor and Francis: New York, NY, USA, 2016; pp. 2169–2181. [CrossRef]
23. Ghosh, G.; Olson, G.B. Precipitation of paraequilibrium cementite: Experiments, and thermodynamic and kinetic modeling. *Acta Mater.* **2002**, *50*, 2099–2119. [CrossRef]
24. Dudko, V.; Yuzbekova, D.; Gaidar, S.; Vetrova, S.; Kaibyshev, R. Tempering Behavior of Novel Low-Alloy High-Strength Steel. *Metals* **2022**, *12*, 2177. [CrossRef]

25. Mishnev, R.; Borisova, Y.; Gaidar, S.; Kniaziuk, T.; Vagina, O.; Kaibyshev, R. Q&P Response of a Medium Carbon Low Alloy Steel. *Metals* **2023**, *13*, 689. [CrossRef]
26. Tkachev, E.; Borisov, S.; Borisova, Y.; Kniaziuk, T.; Gaidar, S.; Kaibyshev, R. Strength–Toughness of a Low-Alloy 0.25C Steel Treated by Q&P Processing. *Materials* **2023**, *16*, 3851. [CrossRef]
27. Kitahara, H.; Ueji, R.; Tsuji, N.; Minamino, Y. Crystallographic features of lath martensite in low-carbon steel. *Acta Mater.* **2006**, *54*, 1279–1288. [CrossRef]
28. Galindo-Nava, E.; Rivera-Díaz-Del-Castillo, P. A model for the microstructure behaviour and strength evolution in lath martensite. *Acta Mater.* **2015**, *98*, 81–93. [CrossRef]
29. Morsdorf, L.; Kashiwar, A.; Kübel, C.; Tasan, C. Carbon segregation and cementite precipitation at grain boundaries in quenched and tempered lath martensite. *Mater. Sci. Eng. A* **2023**, *862*, 144369. [CrossRef]
30. Maalekian, M.; Kozeschnik, E. A thermodynamic model for carbon trapping in lattice defects. *Calphad* **2008**, *32*, 32650–32654. [CrossRef]
31. Hutchinson, B.; Hagström, J.; Karlsson, O.; Lindell, D.; Tornberg, M.; Lindberg, F.; Thuvander, M. Microstructures and hardness of as-quenched martensites (0.1–0.5%C). *Acta Mater.* **2011**, *59*, 5845–5858. [CrossRef]
32. Wilde, J.; Cerezo, A.; Smith, G.D.W. Three-dimensional atomic-scale mapping of a Cottrell atmosphere around a dislocation in iron. *Scripta Mater.* **2000**, *43*, 39–48. [CrossRef]
33. Kamikawa, N.; Huang, X.; Tsuji, N.; Hansen, N. Strengthening mechanisms in nanostructured high-purity aluminium deformed to high strain and annealed. *Acta Mater.* **2009**, *57*, 4198–4208. [CrossRef]
34. Malopheyev, S.; Kulitskiy, V.; Kaibyshev, R. Deformation structures and strengthening mechanisms in an Al-Mg-Sc-Zr alloy. *J. Alloys Compd.* **2017**, *698*, 957–966. [CrossRef]
35. Dudko, V.; Belyakov, A.; Kaibyshev, R. Evolution of Lath Substructure and Internal Stresses in a 9% Cr Steel during Creep. *Iron Steel Inst. Jpn. Int.* **2017**, *57*, 540–549. [CrossRef]
36. Galindo-Nava, E.I.; Rainforth, W.M.; Rivera-Díaz-del-Castillo, P.E.J. Predicting microstructure and strength of maraging steels: Elemental optimisation. *Acta Mater.* **2016**, *117*, 270–285. [CrossRef]
37. Lu, W.; Herbig, M.; Liebscher, C.H.; Morsdorf, L.; Marceau, R.K.W.; Dehm, G.; Raabe, D. Formation of eta carbide in ferrous martensite by room temperature aging. *Acta Mater.* **2018**, *158*, 297–312. [CrossRef]
38. Wang, T.; Du, J.; Liu, F. Modeling competitive precipitations among iron carbides during low-temperature tempering of martensitic carbon steel. *Materialia* **2020**, *12*, 100800. [CrossRef]
39. Pierce, D.T.; Coughlin, D.R.; Williamson, D.L.; Clarke, K.D.; Clarke, A.J.; Speer, J.G.; De Moor, E. Characterization of transition carbides in quench and partitioned steel microstructures by Mössbauer spectroscopy and complementary techniques. *Acta Mater.* **2015**, *90*, 417–430. [CrossRef]
40. Hirotsu, Y.; Nagakura, S. Crystal structure and morphology of the carbide precipitated from martensitic high carbon steel during the first stage of tempering. *Acta Metall.* **1972**, *20*, 645–655. [CrossRef]
41. Bhadeshia, H.K.D.H. *Physical Metallurgy of Steels in Physical Metallurgy*; Laughlin, D.E., Hono, K., Eds.; Elsevier: Amsterdam, The Netherlands, 2014; pp. 2157–2214. [CrossRef]
42. Vengrenovitch, R.D. On the Ostwald ripening theory. *Acta Metall.* **1982**, *30*, 1079–1086. [CrossRef]
43. Wang, L.J.; Cai, Q.W.; Wu, H.B.; Yu, W. Effects of Si on the stability of retained austenite and temper embrittlement of ultrahigh strength steels. *Int. J. Miner. Metall. Mater.* **2011**, *18*, 543–550. [CrossRef]
44. Chaouadi, R.; Gèrard, R. Development of a method for extracting fracture toughness from instrumented Charpy impact tests in the ductile and transition regimes. *Theor. Appl. Fract. Mech.* **2021**, *115*, 103080. [CrossRef]
45. Knott, J.F. *Fundamentals of Fracture Mechanics*; The Butterworth Group: London, UK, 1973.
46. Wang, Q.; Ye, Q.; Wang, Z.; Kan, L.; Wang, H. Thickness Effect on Microstructure, Strength, and Toughness of a Quenched and Tempered 178 mm Thickness Steel Plate. *Metals* **2020**, *10*, 572. [CrossRef]
47. Hanamura, T.; Yin, F.; Nagai, K. Ductile-Brittle Transition Temperature of Ultrafine Ferrite/Cementite Microstructure in a Low Carbon Steel Controlled by Effective Grain Size. *ISIJ Int.* **2004**, *44*, 610–617. [CrossRef]
48. Inoue, T.; Qiu, H.; Ueji, R.; Kimura, Y. Ductile-to-Brittle Transition and Brittle Fracture Stress of Ultrafine-Grained Low-Carbon Steel. *Materials* **2021**, *14*, 1634. [CrossRef]
49. Morris, J.W. On the Ductile-Brittle Transition in Lath Martensitic Steel. *ISIJ Int.* **2011**, *51*, 1569–1575. [CrossRef]
50. Zia-Ebrahimi, F.; Krauss, G. Mechanisms of Tempered Martensite Embrittlement in Medium Carbon Steels. *Acta Metall.* **1984**, *32*, 1767–1777. [CrossRef]
51. Mills, K.; Davis, J.R.; Destefani, J.D.; Dieterich, D. (Eds.) *ASM Handbook, Fractography*; ASM International: Materials Park, OH, USA, 1987; Volume 12.
52. Yuzbekova, D.; Dudko, V.; Kniaziuk, T.; Kaibyshev, R. Effect of tempering on structure and mechanical properties of an ultra-high-strength steel. *Mater. Sci. Eng. A*, 2023; *submitted for publication*.
53. Clarke, A.J.; Speer, J.G.; Miller, M.K.; Hackenberg, R.E.; Edmonds, D.V.; Matlock, D.K.; Rizzo, F.C.; Clarke, K.D.; De Moor, E. Carbon Partitioning to Austenite from Martensite or Bainite during the Quench and Partition (Q&P) Process: A Critical Assessment. *Acta Mater.* **2008**, *56*, 16–22. [CrossRef]

54. Shibata, A.; Katsuno, T.; Tsuboi, M.; Tsuji, N. Effect of Bain unit size on low-temperature fracture toughness in medium-carbon martensitic and bainitic steels. *Int. Iron Steel Inst. Jpn.* **2023**. [CrossRef]
55. Mishnev, R.; Dudova, N.; Dudko, V.; Kaibyshev, R. Impact toughness of a 10% Cr steel with high boron and low nitrogen contents. *Mater. Sci. Eng. A* **2018**, *730*, 1–9. [CrossRef]